



# Degradation phenomena in a solid oxide electrolysis cell after 9000 h of operation

F. Tietz<sup>a,\*</sup>, D. Sebold<sup>a</sup>, A. Brisse<sup>b</sup>, J. Schefold<sup>b</sup>

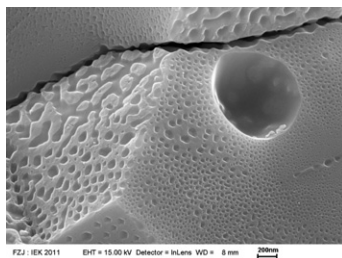
<sup>a</sup> Institute of Energy and Climate Research (IEK-1), Forschungszentrum Jülich GmbH, D-52425 Jülich, Germany

<sup>b</sup> European Institute for Energy Research (EIFER), Emmy-Noether-Strasse 11, D-76131 Karlsruhe, Germany

## HIGHLIGHTS

- ▶ Longest SOEC test to date with comparatively low degradation rate.
- ▶ Solid electrolyte shows internal pore formation due to cation transport.
- ▶ Perovskite anode shows compositional inhomogeneities and cation de-mixing.
- ▶ Interface between Ni/YSZ cathode and electrolyte is destabilised due to materials transport towards the anode.

## GRAPHICAL ABSTRACT



## ARTICLE INFO

### Article history:

Received 12 June 2012

Received in revised form

7 September 2012

Accepted 17 September 2012

Available online 23 September 2012

### Keywords:

High-temperature steam electrolysis

SOEC

Long-term testing

Degradation

Post-test analysis

## ABSTRACT

An anode-supported solid oxide fuel cell (SOFC) was operated for 9000 h as a solid oxide electrolyser cell (SOEC) with a current density of  $-1 \text{ Acm}^{-2}$  showing a voltage increase of about  $40 \text{ mV kh}^{-1}$ , i.e. an overall voltage degradation rate of  $3.8\% \text{ kh}^{-1}$ . The cell consisted of yttria-stabilised zirconia (YSZ) combined with a gadolinia-substituted ceria layer as electrolyte. The hydrogen electrode was a Ni/YSZ cermet, and the oxygen electrode a  $\text{La}_{0.58}\text{Sr}_{0.4}\text{Co}_{0.2}\text{Fe}_{0.8}\text{O}_3$  perovskite (LSCF). After electrolysis operation, the cell was metallographically analysed to identify degradation processes. Compared with the initial state, the most pronounced change was found at the electrolyte layer, which showed trans-granular longitudinal porosity as well as severe pore formation along grain boundaries. In addition, material transport was observed into the ceria-based diffusion barrier layer. The oxygen electrode showed compositional variations in the sub- $\mu\text{m}$  range and different degrees of recrystallisation across the electrode thickness. The microstructural observations agree with the already reported impedance spectroscopic results, which indicated (i) an increase in ohmic electrolyte resistance as the dominant degradation feature, which is specific to SOEC operation, and (ii) an increase in the electrode reaction overpotentials.

© 2012 Elsevier B.V. All rights reserved.

## 1. Introduction

High-temperature solid oxide cells (SOCs) can be reversibly operated as fuel cells (SOFCs) and as electrolyser cells (SOECs) for water splitting or syngas production. SOECs allow high electrical-to-chemical energy conversion efficiencies [1–3], making high temperature electrolysis very attractive for the production of

hydrogen or syngas in the context of renewable energy conversion and storage (“power2gas”). There has been significant technical progress with respect to SOFC development during the last three decades [4–6] and SOEC application is expected to benefit to a large extent from this progress. Hence, the technology is rapidly growing at present due to the fact that many SOFC manufacturers see the opportunity for an additional application. The two operating modes, however, differ in the applied potential gradients, which affect performance and long-term stability.

In recent years, many efforts have been made to understand the processes during SOFC and SOEC operation determining the

\* Corresponding author. Tel.: +49 2461 615007; fax: +49 2461 612455.

E-mail address: [f.tietz@fz-juelich.de](mailto:f.tietz@fz-juelich.de) (F. Tietz).

deterioration of cell voltage over time. Very recently, the degradation phenomena have been extensively compiled and described [7]. Among these phenomena, the following degradation processes have only been observed in electrolysis mode, primarily due to the larger  $p(\text{O}_2)$  gradient across the electrolyte [8], resulting in a stronger driving force for diffusion processes [9,10]. This might cause additional degradation features to those known from SOFC operation [7,11,12]:

- enhanced diffusion processes in the electrolyte and the formation of Kirkendall voids [9,13],
- formation of oxygen in the electrolyte [14],
- different oxygen activity in the oxygen electrode and hence different catalytic activity for oxygen reduction and oxygen evolution as SOFC and SOEC, respectively,
- delamination or microstructure degradation of the electrolyte/oxygen electrode interface [2,15–18],
- enhanced evaporation of  $\text{Ni}(\text{OH})_2$  due to higher  $p(\text{H}_2\text{O})$  in the fuel gas [7]
- enhanced silicon poisoning of the hydrogen electrode due to higher  $p(\text{H}_2\text{O})$  [19,20].

So far, SOECs have not been operated for extended periods. Therefore the degradation phenomena are often hard to detect. Moreover, they depend on the testing conditions (current density, steam content in the fuel gas, steam conversion rate, temperature). Besides the cell reported here, the longest reported cell test lasted for 2000 h at  $j = -0.3 \text{ Acm}^{-2}$  of a  $12.5 \text{ cm}^2$  metal-supported cell [21] and showed a degradation rate of  $3.2\% \text{ kh}^{-1}$ . Stack degradation tends to be faster than cell degradation due to additional impacts from the piping, interconnects and seals [12,18,22,23]. Degradation rates between 3 and  $7\% \text{ kh}^{-1}$  were reported for short stack tests of up to 5000 h [3,24,25].

The cell tested in the present work was operated for 9000 h [26] with the aim of clearly identifying degradation issues during steady electrolysis operation. The same type of cell has also been operated for up to 17,000 h in SOFC mode [27,28] and therefore makes it possible to identify the differences in degradation mechanisms between the two types of applications.

## 2. Experimental

A circular anode-supported SOFC from Forschungszentrum Jülich with an active cell area of  $45 \text{ cm}^2$  was used. The electrolyte consisted of a dense layer of 8 mol% yttria-stabilised zirconia (8YSZ) with a thickness of  $10 \mu\text{m}$  and a porous diffusion barrier layer of  $\text{Ce}_{0.8}\text{Gd}_{0.2}\text{O}_{1.9}$  (CGO)  $5 \mu\text{m}$  in thickness. The oxygen electrode was made of  $\text{La}_{0.58}\text{Sr}_{0.4}\text{Co}_{0.2}\text{Fe}_{0.8}\text{O}_3$  (LSCF) with a thickness of 35–40  $\mu\text{m}$ . The steam/hydrogen electrode was a Ni/8YSZ cermet (8  $\mu\text{m}$  thickness) on a 1.5 mm thick Ni/8YSZ anode substrate. The processing of such cells has been described elsewhere [29,30].

The experimental setup for the cell test was reported in [26]. In brief, the measurement was carried out in a test bench with an unsealed alumina housing configuration using platinum and nickel meshes as current collectors. The sweep gas to the oxygen electrode consisted of  $90 \text{ NI h}^{-1}$  synthetic air. The gas to the SOEC cathode consisted of  $6 \text{ NI h}^{-1} \text{ H}_2$ ,  $7.08 \text{ NI h}^{-1} \text{ N}_2$ , and  $42 \text{ g h}^{-1}$  steam corresponding to an absolute humidity of 80 vol.%. The current density was  $j = -1 \text{ Acm}^{-2}$  resulting in a steam utilisation of 36%. The cell temperature was  $778 \pm 6^\circ\text{C}$ . Cell impedance was recorded without interruption of the steady-state DC current flow.

For post-test analysis, the cell was broken to investigate the fracture surfaces. Parts of the cell were embedded and infiltrated with resin and polished to obtain flat cross sections of all cell components. The samples were investigated in detail using

scanning electron microscopy (SEM, Ultra 55, Zeiss, Oberkochen, Germany) and energy-dispersive X-ray analysis (EDX, INCA, Oxford Instruments, Oxford, UK).

## 3. Results and discussion

The recently reported [26] cell performance during 9000 h of operation included the voltage–current ( $U$ – $j$ ) behaviour as well as the cell impedance under steady-state operation with an applied current of  $-1 \text{ Acm}^{-2}$ . The voltage increase over the entire experiment was  $3.8\%$  ( $40 \text{ mV kh}^{-1}$ ). This degradation value accounts not only for cell-related phenomena but also for experimental incidents, especially during the period of 7600–9200 h of operation caused by supply failures of steam or feed gas. The degradation rate during the initial 7600 h was  $3.0\%$  ( $32 \text{ mV kh}^{-1}$ ) (Fig. 1).

In the following, the results from the post-test analysis of electrolyte and electrodes are first discussed and then linked to the electrochemical observations during the test.

### 3.1. Electrolyte

Fig. 2 shows the microstructure of the cell after testing. At the given magnification, no special features are visible apart from the pronounced grain structure of the electrolyte indicating a fracture mode along grain boundaries. This is unusual compared with fracture surfaces of as-prepared or operated SOFCs [31], which typically show an intragranular fracture of the electrolyte. The reason for the intergranular fracture observed here becomes visible at higher magnification (Fig. 3). On the surface of each grain a varying structuring is observed depending on the crystal orientation. On the grain surfaces, rectangular, hexagonal and also pentagonal voids are formed in sizes of 5–50 nm. When such voids become larger and combine with each other, irregular structures result (cf. Fig. 3c). The change of the surface structure has two consequences: loss of mechanical stability and loss of contact area. The reduced fracture strength is not only responsible for the intergranular fracture surface but is also a critical point during operation as soon as mechanical stresses are induced by thermal cycles or changing operating conditions leading to different temperature gradients across the cell or stack. The loss of contact area means an increase of contact resistance. Therefore this phenomenon contributes significantly to the voltage increase observed during the electrolysis test.

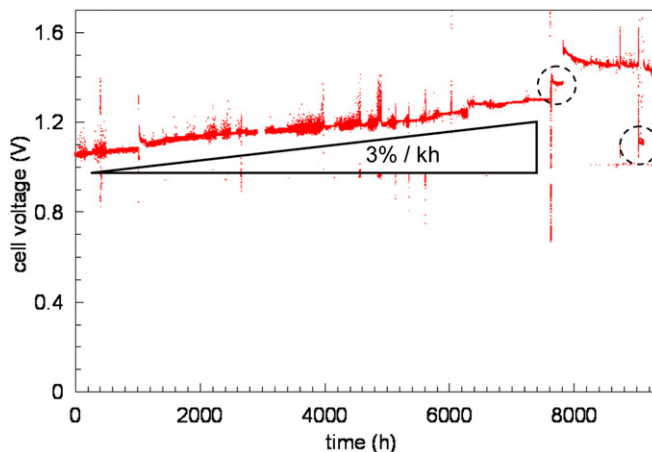
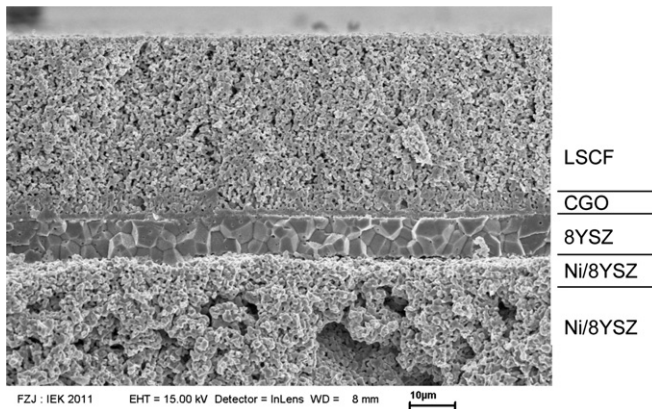


Fig. 1. Cell voltage during operation with  $j = -1.0 \text{ Acm}^{-2}$ . Longer periods of derated current density are marked by circles and indicate malfunctions of the steam evaporator causing activation of overvoltage protection at lower current density.



**Fig. 2.** Microstructure of tested SOEC at low magnification. From top to bottom: LSCF anode, CGO barrier layer, 8YSZ electrolyte, Ni/8YSZ cathode, Ni/8YSZ substrate.

A similar observation, but to a much smaller extent, due to the shorter period of electrolysis operation, was reported by Knibbe et al. [14], who investigated areas of the electrolyte near the oxygen electrode by transmission electron microscopy. They found pores along grain boundaries accompanied by a chemical gradient of Zr and Y ions. The nm-sized pore formation was restricted to individual grain boundaries close to the oxygen electrode/electrolyte interface.

A second difference from the original microstructure of the electrolyte layer is the horizontally aligned pores throughout the electrolyte (Fig. 3a–c) indicated by the arrows in Fig. 3b and c. The number of pore layers is high at the 8YSZ/CGO interface (Fig. 4a) and decreases with increasing distance from this interface. The occurrence is not only a function of the diffusion length, but also seems to be influenced by the orientation of the YSZ grains. Considering an electrochemical potential gradient perpendicular to the electrolyte layer, the differently oriented grain surfaces are exposed to a varying, angle-dependent potential strength which is phenomenologically visible as surface-dependent void structure on the grain surfaces (Fig. 3d). With increasing operation time in electrolysis mode this orientation-dependent structuring of grain boundaries increases and leads to different contact areas between the grains and hence to different contact resistances. The origin of the pore layers is likely due to the cation diffusion in the electrolyte, which is stimulated by the larger  $p(\text{O}_2)$  gradient, i.e. the larger electrochemical potential [9,10,32], as mentioned above but "scattered" due to the varying contact resistances leading to pore formation in different depths of the electrolyte layer. The mass transport of two or more species with different mobility leaves pores behind, the so-called Kirkendall voids [33,34]. As a consequence, the material that has moved from the electrolyte interior has to be deposited elsewhere. Indeed, the cation diffusion led to the formation of a dense layer at the 8YSZ/CGO interface (Figs. 3a,3b,4a), which has a thickness of about 1.5  $\mu\text{m}$ . From the

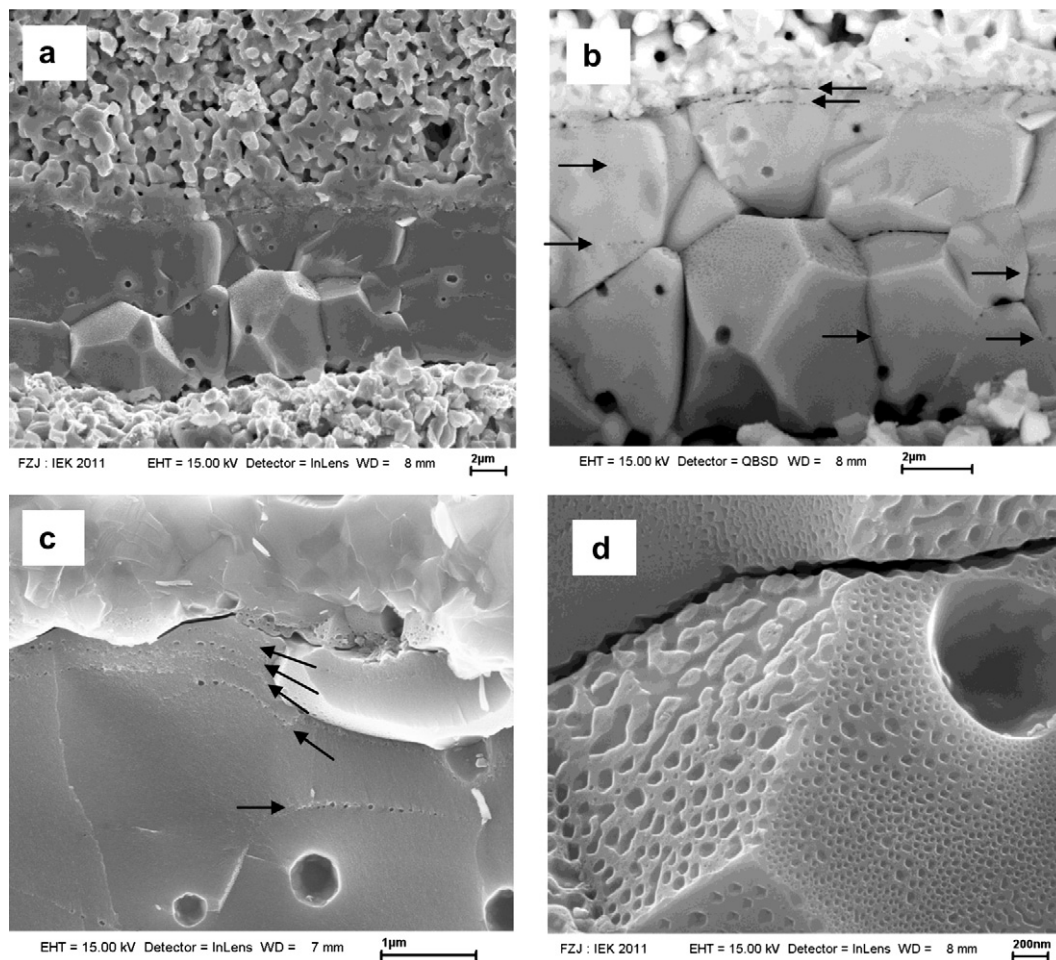


**Fig. 3.** Images of fracture surfaces of the electrolyte layer. (a) Area of inter- and intragranular fracture, (b) same region in back-scattering mode showing more clearly horizontally structured pores (arrows) over the entire electrolyte layer and (c) at the CGO/YSZ interface, (d) highly enlarged 8YSZ grain surface with fractured grain boundary.



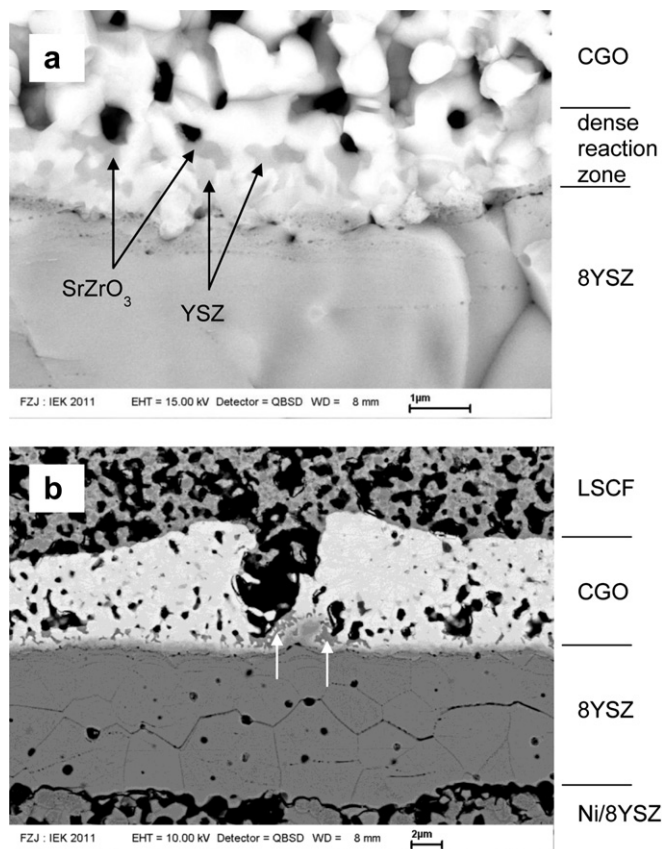


**Fig. 4.** Back-scattering images of the 8YSZ/CGO interface. (a) Enlarged area of Fig. 3b showing the formation of SrZrO<sub>3</sub>, the diffusion of YSZ into the CGO layer and the horizontal pore structure along the interface, (b) Enhanced SrZrO<sub>3</sub> formation (arrows) at positions of sintering cracks in the CGO layer, where the cathode can be in direct contact with YSZ. The grey scale gradient at the 8YSZ/CGO interface indicates the diffusion of Zr and Y into the CGO layer.

high-resolution back-scattering image (Fig. 4a) three different phases can be distinguished due to the different grey scale values resulting from the different mean atomic numbers of the atoms involved. The white phase is CGO, the light grey phase is YSZ and the phase with darker grey scale is SrZrO<sub>3</sub> as confirmed by EDX analyses. It is interesting to note that the SrZrO<sub>3</sub> only appears at positions with direct contact to the pore structure of the CGO layer indicating that the strontium can only have arrived at this region by surface or gas diffusion [27]. Whereas SrZrO<sub>3</sub> formation is known and can occur during sintering [29], the difference from previous observations is in this case the appearance of grains not directly at the 8YSZ/CGO interface but at a distance of about 1 μm. This implies two possible ways in which SrZrO<sub>3</sub> can have reacted as shown in Fig. 4a. Either the SrZrO<sub>3</sub> grains were not present after manufacturing and have formed during electrolysis by reaction of Sr with the outward diffusion of zirconia, or the SrZrO<sub>3</sub> grains were formed during cell manufacturing at the interface and were shifted into the CGO layer by the diffusing zirconia. Additional experiments with a dense CGO layer [35] should be able to clarify the mechanism. However, in both cases the diffusion of zirconia into the CGO layer is necessary to explain the position of the SrZrO<sub>3</sub> grains.

The polished cross section in Fig. 4b shows a vertical gap in the CGO layer, which can occur during sintering. Depending on the sintering temperature and shrinkage of the CGO paste during the constraint sintering on the electrolyte layer, crack formation is a typical artefact of this processing step. In these areas, the LSCF can easily come into direct contact with the 8YSZ electrolyte leading to

enhanced formation of SrZrO<sub>3</sub>. As shown in this figure, the diffusion of zirconia also seems to be more enhanced because there is an excrescence of zirconia between the two areas of SrZrO<sub>3</sub> (see arrows pointing to the dark grey regions). It is also worth noting that this cross-sectional view clearly visualizes the weak bonds between the electrolyte grains and poor contact at the electrolyte/cathode interface at the bottom part of Fig. 4b. This detachment of Ni grains has also been observed recently, but was limited to single grains [14].

### 3.2. Oxygen electrode (anode)

At low magnification, the microstructure of the LSCF anode seems to be unaffected by the long electrolysis test (Fig. 2). However, the fracture surfaces hide the chemical changes that occurred during testing. Only the polished cross sections (Figs. 4b and 5) in combination with the back-scattering mode in SEM investigation give clear evidence for compositional changes in the LSCF. As shown in Fig. 5, the LSCF framework is not homogeneous but is composed of stoichiometric fluctuations in the sub-μm range indicated by different back-scattering intensities. Unfortunately, the elemental variation is too small to be analysed by SEM/EDX and more investigations with higher local resolution are necessary to elucidate the stoichiometric changes. Nevertheless, the change of the perovskite composition can be indirectly analysed by X-ray diffraction (Fig. 6). The diffraction pattern after the electrolysis test clearly shows the broadening of reflections towards smaller diffraction angles and the appearance of very small additional reflections at  $2\theta = 30.3, 31.4$  and  $44.7^\circ$ , which can be attributed to the formation of Co<sub>3</sub>O<sub>4</sub>. The broadening of the reflections clearly indicates the inhomogeneity of the electrode and the existence of various perovskite compositions that have formed during operation. On the larger scale, no significant gradients across the thickness of the electrode were detected, in contrast to results obtained from a post-test analysis of an SOFC after long-term operation [28], where a pronounced depletion of Sr towards the outer electrode surface was observed.

In addition to the chemical changes also a morphological change was observed across the LSCF electrode. Whereas the LSCF particles at the outer part of the electrode—close to the current collector—are round and tend to be individually attached to each other, the LSCF particles at the centre and especially towards the electrolyte show many more crystal faces and edges (Fig. 7). It seems that the perovskite minimises the surface defects and re-crystallises under the influence of the electrochemical gradient.

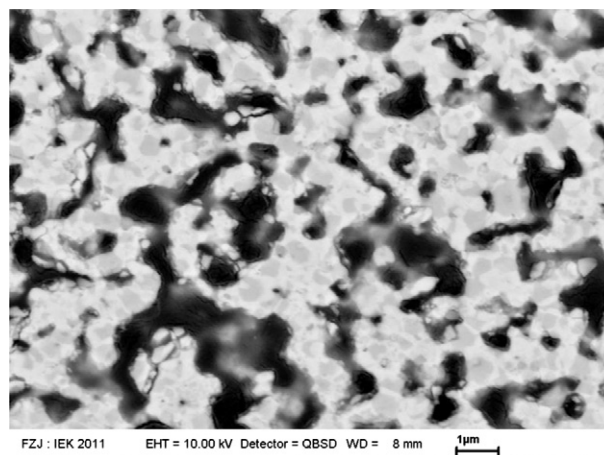


**Fig. 5.** Back-scattering image of a polished cross section of the LSCF anode.

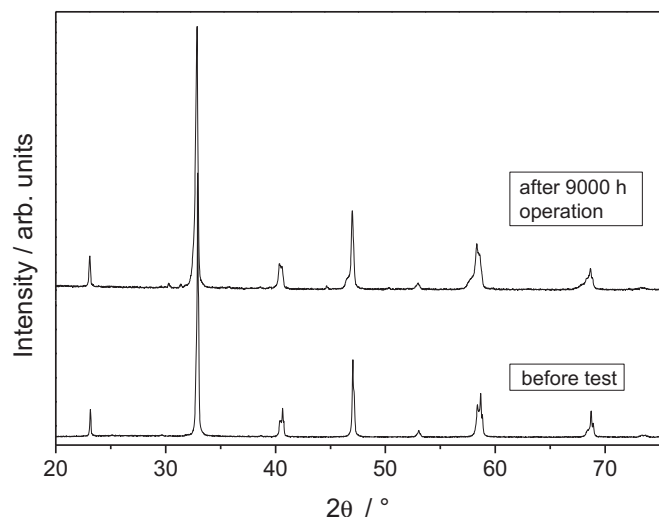


**Fig. 6.** X-ray diffraction pattern (Cu  $K_\alpha$  radiation) of LSCF anode before testing (bottom) and after 9000 h of operation in electrolysis mode (top).

### 3.3. Hydrogen electrode (cathode)

The hydrogen electrode is the component with the smallest changes after the electrolysis test. The surface decoration of the 8YSZ

grains, as discussed above, is also visible in the cathode. However, the surface structures diminish at a distance of about 10–20  $\mu\text{m}$  from the electrolyte interface. Directly at the electrolyte, the contact to the hydrogen electrode seems to be weakened as shown in Fig. 4b and also observed at several other positions along the interface.

As in the oxygen electrode, there is a morphological change of the catalyst particles as a function of distance from the electrochemically active region. Directly at the electrolyte interface, the Ni particles have a rough surface (Fig. 8a). The surface roughness continuously decreases, and at the centre of the substrate the Ni particles are smooth and round with nano-sized dendrites on the surface (Fig. 8b). These dendrites only exist on the Ni particles and not on the 8YSZ grains.

In contrast to earlier post-test analyses [19,20], impurity segregations at the electrolyte/hydrogen electrode interface were not observed.

### 3.4. Comparison of microstructural and electrochemical results

The post-test features correlate with the cell degradation observed during the long-term test, although the quantitative contribution of each feature may be difficult to establish. Neglecting the contacting issues between oxygen electrode and Pt mesh (cf. [26]), the increase in cell voltage can be a consequence of (i) decreasing ionic conduction in the electrolyte, (ii) decreasing electronic conduction in the electrodes, (iii) electrode deactivation, and

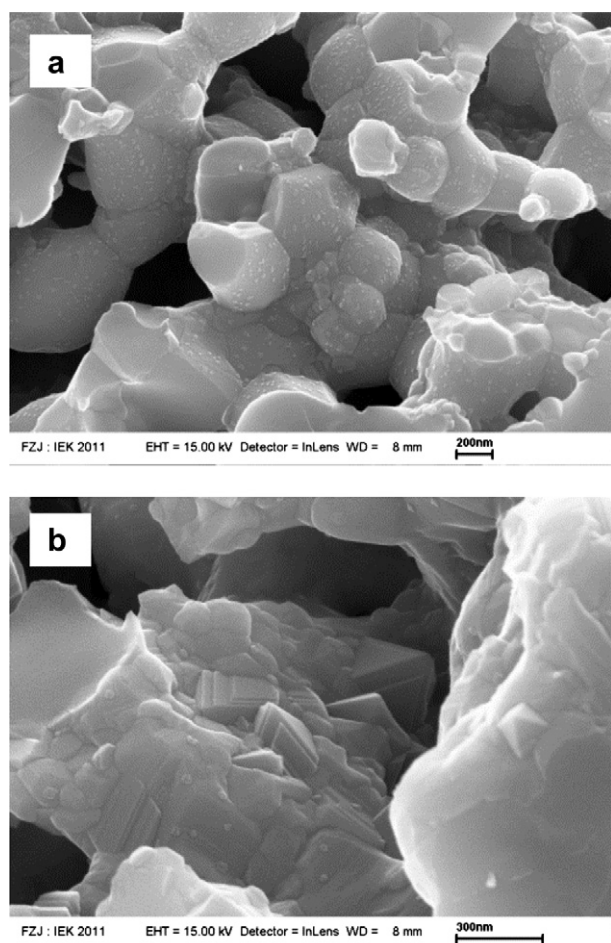


**Fig. 7.** Gradual changes of surface structures across the LSCF air electrode: (a) at the outer surface round particles with nano-sized surface structure, (b) at the centre and at the electrolyte many crystallites with sharp edges and crystal faces.

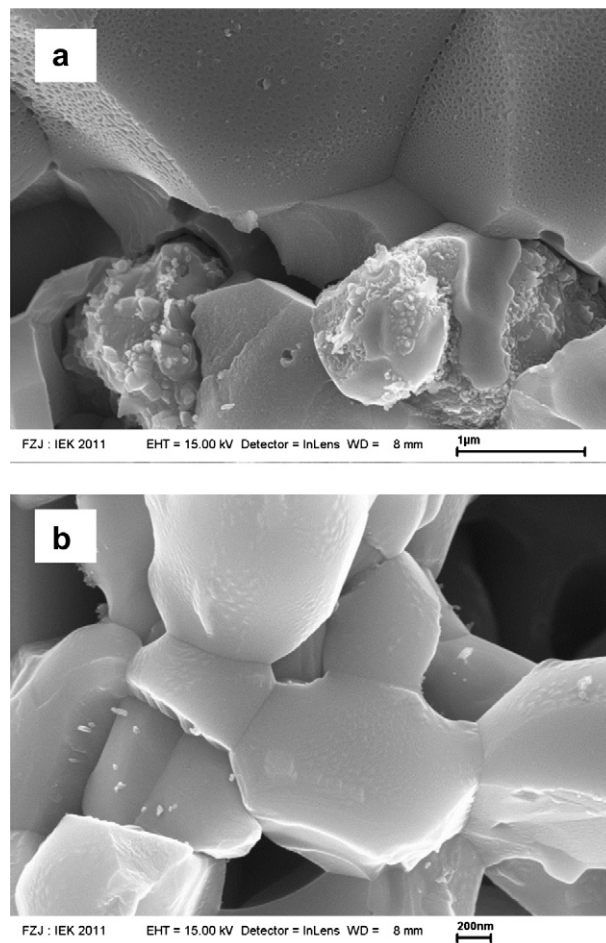


**Fig. 8.** Gradual changes of surface structures across the Ni/8YSZ fuel electrode: (a) Ni particles at the electrolyte interface have a rough surface, (b) at the centre of the substrate the Ni particles are smooth and round with nano-sized dendrites on the surface.

(iv) increasing cell resistance due to the formation of layers of low conductivity or layer delamination. Impedance spectroscopy (IS) distinguishes the main relaxation features of the electrode reactions and separates them from the ohmic terms (ohmic terms from different sources are not distinguishable in impedance). For the initial part of the 9000 h test, the impedance plots after 21 and 1266 h of operation are shown in Fig. 9. The results from IS characterisation, presented and discussed in more detail in [26], are briefly recapitulated here. Cell impedance increased with operating time, in accordance with the increase in cell voltage and cell ASR [26] due to:

1. an increase in the ohmic contributions seen at high-frequency resistance ( $R_{HF}$ ), as a sum of the ionic electrolyte resistance ( $R_{ion(YSZ)}$ ) resulting from increasing resistances of potential barrier layers and contacting. The  $R_{HF}$  value rose from an initial  $R_{HF} \approx 0.08 \Omega\text{cm}^2$  to about  $0.33 \Omega\text{cm}^2$  after 9200 h total operating time, equivalent to about 50% of the total increase in the differential cell resistance.
2. an increase in the non-ohmic contributions above about 300 Hz, the range of interfacial charge transfer processes at the electrodes. No distinction in anode or cathode deactivation could be made, but there are indications for  $\text{H}_2\text{O}/\text{H}_2$  electrode deactivation from related work.
3. a minor increase in the low-frequency (0.1–10 Hz) contribution indicating an emerging mass transport limitation. This result

agrees with a slope increase of the  $U$ – $j$  curve around the nominal current density after prolonged operation.

Point 1: The post-test analysis of the electrolyte confirms the crucial role of this cell component which makes the largest contribution to overall SOEC degradation according to the IS results. The loss in granular contact area together with the pore formation explains a rising ohmic resistance. The structural changes may also have affected the specific ionic conductivity of the electrolyte. The resistance continuously increased during the test without reaching a limiting value. Although a weakening of the mechanical properties of the electrolyte is clearly indicated, no electrolyte failure was observed due to SOEC operation verified by a stable open circuit voltage. Cell fissuring after 7600 h was induced by blocking of feed gas supply, i.e. due to an experimental incident. Moreover, the electrolyte survived operating periods under steam starvation and electronic current flow, which means cell voltages approaching 2 V and the corresponding very low oxygen partial pressures at the cathode side. This is in agreement with reported intentional cell operation in the electronic conduction mode of the electrolyte [36].

Point 2: The post-test data indicate that oxygen-electrode deactivation plays a more important role than originally assumed. Both the compositional fluctuations and the morphological changes agree with a loss of catalytic activity of this electrode. For a better and more quantitative separation of anode and cathode processes, an appropriate electrochemical characterisation has to be established and implemented in the testing procedure.

Electrode degradation may coincide with an increase in electronic resistance of the electrodes. However, this resistance is far below the ionic resistance of the electrolyte, and its increase may be masked by the larger and more easily detectable impedance increase caused by a loss of catalytic electrode activity.

Point 3: The minor increase in the voltage losses due to mass transport can be attributed to small changes in porosity of the electrochemically active Ni in the  $\text{H}_2\text{O}/\text{H}_2$  electrode. As this voltage loss is small, it agrees well with the observation that no significant detectable agglomeration of the Ni particles occurred. Indirectly, this increase implies that most likely also the catalytic activity of the electrode changes with time.

For a comparison of in-test and post-test results, it has to be kept in mind that the post-test features may not only originate from 'normal' SOEC operation but also from operational incidents [26]. The reported increase in contact resistance from the cell electrodes to the cell housing (due to mechanical shocks) is not expected to influence the post-test analysis significantly, as it only yields minor changes in the cell temperature. The temperature increase and temperature cycling is more significant during the periods with disturbed steam supply or steam-supply failure. The temperature changes are caused by higher cell voltages due to increased steam conversion rates, or, without sufficient steam supply, by Joule heating from electronic current flow across the electrolyte. Electronic current flow in the electrolyte, moreover, implies the lowest oxygen partial pressures at the  $\text{H}_2\text{O}/\text{H}_2$  electrode [35], and it is not known how this affects the electrolyte morphology. Finally, an even stronger impact on the cell morphology is expected from the periods of supply failure of the  $\text{H}_2\text{O}/\text{H}_2$  feed gas. The first incident of this kind after 7600 h of operation led to minor cell fissuring and partial re-oxidation of the  $\text{H}_2\text{O}/\text{H}_2$  electrode. These operational incidents may have contributed notably to the cracking or delamination features seen in the post-test analysis.

#### 4. Conclusions

Long-term operation at a current density  $j = -1 \text{ Acm}^{-2}$  in the electrolysis mode of a hydrogen-electrode-supported SOC caused several changes in the cell materials:

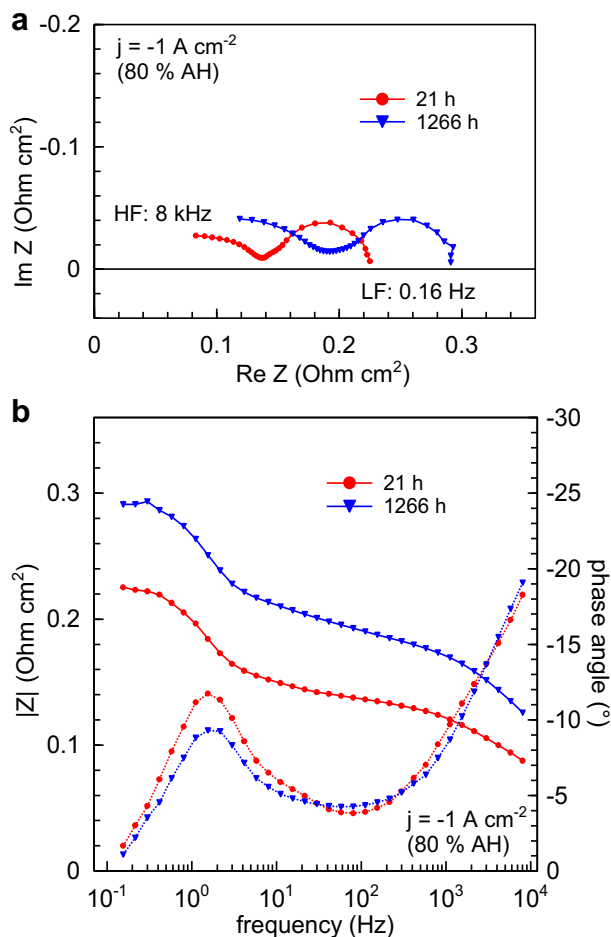


Fig. 9. Cell impedance after 21 and 1266 h operation taken at steady-state DC current density of  $j = -1 \text{ Acm}^{-2}$  as (a) Cole–Cole plots and (b) magnitude/phase presentation. Results for the entire test run are reported in [26].



- a) structuring of grain surfaces in the electrolyte, void formation along grain boundaries (affecting mechanical properties and ohmic resistance)
- b) horizontally aligned pores, especially at the 8YSZ/CGO interface
- c) mass transport and formation of a dense layer at the 8YSZ/CGO interface
- d) compositional fluctuations in the LSCF electrode (affecting the ohmic resistance)
- e) re-crystallisation of LSCF in the electrochemically active area (affecting the catalytic behaviour of the electrode)
- f) destabilisation of the 8YSZ/Ni-YSZ interface (affecting the mechanical properties)
- g) varying surface roughness of the Ni particles

In view of these degradation phenomena, the increase in cell voltage of  $3\% \text{ kh}^{-1}$  is rather small. At this point, it is not possible to allocate all specific fractions of the degradation rate to the processes listed above. It is, however, reasonable to assume that process a) directly causes an increase of the ohmic part of the area-specific cell resistance. Impedance spectroscopic measurements have shown that this process has the strongest impact on cell degradation. Also process e) plays an important role for the catalytic activity of the electrode leading to changes in the polarisation resistance. Processes a) and f), as a result of mass transport of zirconia from the fuel to the oxygen compartment, do not only contribute to the electrochemical properties of the cell, but also significantly reduce the mechanical strength of the cell. This can have an impact on lifetime, when thermal cycling and abrupt changes of operating conditions are considered.

## Acknowledgements

The authors gratefully acknowledge M. Kappertz and M. Peterlick (both IEK-1, Forschungszentrum Jülich) for technical assistance and X-ray diffraction measurements, respectively, and Dr. M. Schroeder (IPC, RWTH Aachen) for helpful discussions. The work was financially supported by the Federal Ministry of Economics and Technology under contract no. 03ET2014.

## References

- [1] W. Doenitz, R. Schmidberger, E. Steinheil, R. Streicher, *Int. J. Hydrog. Energy* 5 (1980) 55–63.
- [2] A. Hauch, S.H. Jensen, S. Ramousse, M. Mogensen, *J. Electrochem. Soc.* 153 (2006) A1741–A1747.
- [3] M. Zahid, J. Schefold, A. Brisse, in: D. Stolten (Ed.), *Hydrogen and Fuel Cells, Fundamentals, Technologies and Applications*, Wiley-VCH, Weinheim, Germany, 2010, pp. 227–242.
- [4] A.O. Isenberg, *Solid State Ionics* 3/4 (1981) 431–437.
- [5] N.Q. Minh, *J. Am. Ceram. Soc.* 76 (1996) 563–588.
- [6] N.H. Menzler, F. Tietz, S. Uhlenbruck, H.-P. Buchkremer, D. Stöver, *J. Mater. Sci.* 45 (2010) 3109–3135.
- [7] R. Knibbe, A. Hauch, J. Hjelm, S.D. Ebbesen, M. Mogensen, *Green* 1 (2011) 141–169.
- [8] T. Jacobsen, M. Mogensen, *ECS Trans.* 13 (26) (2008) 259–273.
- [9] M. Martin, *Solid State Ionics* 136–137 (2000) 331–337.
- [10] M. Martin, *J. Chem. Thermodyn.* 35 (2003) 1291–1308.
- [11] H. Yokokawa, H.Y. Tu, B. Iwanschitz, A. Mai, *J. Power Sources* 182 (2008) 400–412.
- [12] H. Nabelek, L. Blum, H.P. Buchkremer, V.A.C. Haanappel, L.G.J. de Haart, W.J. Quadackers, R. Steinberger-Wilckens, R.W. Steinbrech, U. Reisgen, F. Tietz, *Ceram. Eng. Sci. Proc.* 28 (4) (2009) 65–77.
- [13] M. Kuznecov, P. Otschik, P. Obenaus, K. Eichler, W. Schaffrath, *Solid State Ionics* 157 (2003) 371–378.
- [14] R. Knibbe, M.L. Traulsen, A. Hauch, S.D. Ebbesen, M. Mogensen, *J. Electrochem. Soc.* 157 (2010) B1209–B1217.
- [15] A. Hauch, S.D. Ebbesen, S.H. Jensen, M. Mogensen, *J. Mater. Chem.* 18 (2008) 2331–2340.
- [16] J.S. Herring, J.E. O'Brien, C.M. Stoots, G.L. Hawkes, J.J. Hartvigsen, M. Shahnam, *Int. J. Hydrog. Energy* 32 (2007) 440–450.
- [17] A.V. Virkar, *Int. J. Hydrog. Energy* 35 (2010) 9527–9543.
- [18] J.R. Mawdsley, J.D. Carter, A.J. Kropf, B. Yildiz, V.A. Maroni, *Int. J. Hydrog. Energy* 34 (2009) 4198–4207.
- [19] A. Hauch, S. Højgaard Jensen, J.B. Bilde-Sørensen, M. Mogensen, *J. Electrochem. Soc.* 154 (2007) A619–A626.
- [20] A. Hauch, S.D. Ebbesen, S.H. Jensen, M. Mogensen, *J. Electrochem. Soc.* 155 (2008) B1184–1193.
- [21] G. Schiller, A. Ansar, M. Lang, O. Patz, *J. Appl. Electrochem.* 39 (2009) 293–301.
- [22] S. Elangovan, J. Hartvigsen, in: R.H. Jones, G.J. Thomas (Eds.), *Materials for the Hydrogen Economy*, CRC Press, Boca Raton, USA, 2008, pp. 61–80 (Chapter 3).
- [23] V.I. Sharma, B. Yildiz, *J. Electrochem. Soc.* 157 (2010) B441–B448.
- [24] J. Schefold, A. Brisse, M. Zahid, *ECS Trans.* 28 (11) (2010) 357–367.
- [25] J. Schefold, A. Brisse, M. Zahid, J.P. Ouweltjes, J.U. Nielsen, *ECS Trans.* 35 (1) (2011) 2915–2927.
- [26] J. Schefold, A. Brisse, F. Tietz, *J. Electrochem. Soc.* 159 (2) (2012) A137–A144.
- [27] F. Tietz, A. Mai, D. Stöver, *Solid State Ionics* 179 (2008) 1509–1515.
- [28] N.H. Menzler, P. Batfalsky, S.M. Groß, V. Shemet, F. Tietz, *ECS Trans.* 35 (1) (2011) 195–206.
- [29] A. Mai, V.A.C. Haanappel, S. Uhlenbruck, F. Tietz, D. Stöver, *Solid State Ionics* 176 (2005) 1341–1350.
- [30] V.A.C. Haanappel, B. Bär, C. Tropartz, J. Mertens, F. Tietz, *J. Fuel Cell. Sci. Technol.* 7 (2010) 061017.
- [31] J. Malzbender, E. Wessel, R.W. Steinbrech, *Solid State Ionics* 176 (2005) 2201–2203.
- [32] J. Chun, H.-I. Yoo, *J. Korean Ceram. Soc.* 49 (2012) 48–55.
- [33] A.D. Smigelskas, E.O. Kirkendall, *Trans. Am. Inst. Min. Metallurg. Eng.* 171 (1947) 130–142.
- [34] J.D. Kuenzly, D.L. Douglass, *Oxid. Met.* 8 (1974) 139–178.
- [35] A. Mai, V.A.C. Haanappel, F. Tietz, D. Stöver, *Solid State Ionics* 177 (2006) 2103–2107.
- [36] J. Schefold, A. Brisse, M. Zahid, *J. Electrochem. Soc.* 156 (2009) B897–B904.